TSC simulation of Ohmic discharges in TFTR

1993 Nucl. Fusion 33 371

(http://iopscience.iop.org/0029-5515/33/3/I01)

TSC SIMULATION OF OHMIC DISCHARGES IN TFTR

S.C. JARDIN, M.G. BELL, N. POMPHREY
Princeton Plasma Physics Laboratory,
Princeton University,
Princeton, New Jersey,
United States of America

ABSTRACT. The Tokamak Simulation Code (TSC) has been used to model the time dependence of several Ohmic discharges in the TFTR experiment. The semi-empirical thermal conductivity model and the sawtooth model in TSC have been refined so that good agreement between the simulation and the experiment is obtained in the electron and ion temperature profiles and in the current profiles for the entire duration of the discharges. Neoclassical resistivity gives good agreement with the measured surface voltage and the rate of poloidal flux consumption.

1. INTRODUCTION

The Tokamak Simulation Code [1] (TSC) is a two-dimensional time dependent free boundary simulation code that advances the MHD equations describing the transport time-scale evolution of an axisymmetric magnetized tokamak plasma. TSC evolves the magnetic field in a rectangular computational domain using the Maxwell MHD equations for the plasma, coupled through boundary conditions to the circuit equations for the tokamak poloidal field (PF) coils. The plasma model in TSC is completed by providing functional forms for the electron and ion thermal conductivities, for the particle diffusion coefficients and for the plasma electrical resistivity.

A semi-empirical plasma transport model [2–6] is presently utilized in TSC. While having some theoretical and empirical foundations, the model contains several free coefficients, or adjustable parameters, which are chosen so that the predictions of the simulation code agree as closely as possible with the experimental database. We report here on our experience in benchmarking this model against Ohmic discharges in the TFTR experiment.

2. THE TSC MODEL

TSC solves a modified force balance equation on a background Cartesian grid to maintain the plasma in near equilibrium during its evolution [1]. The poloidal flux function Ψ and the toroidal field function g are also evolved on this fixed background grid, where the axisymmetric magnetic field is represented in the standard form

$$\vec{B} = \nabla\phi \times \nabla\Psi + g\nabla\phi \tag{1}$$

with ϕ being the symmetry angle in a cylindrical co-ordinate system (R, ϕ, z).

The evolving magnetic surfaces define a magnetic geometry which changes in time. We use the toroidal flux Φ inside a magnetic surface as the co-ordinate label for that surface. The large ratios of parallel to perpendicular diffusivity and of parallel to perpendicular thermal conductivity permit magnetic surface averaging to obtain one-dimensional transport equations for number and entropy densities,

$$\frac{\partial}{\partial t} N' = -\frac{\partial}{\partial \Phi}(N'\Gamma) + S_N \tag{2}$$

$$\frac{\partial}{\partial t}\sigma = \frac{2}{3}\left(\frac{\partial V}{\partial \Phi}\right)^{2/3}\left[V_L \frac{\partial K}{\partial \Phi} - \frac{\partial}{\partial \Phi}(Q_i + Q_e) + \frac{\partial V}{\partial \Phi}(S_e + S_i - R_e)\right] \tag{3}$$

$$\frac{\partial}{\partial t}\sigma_e = \frac{2}{3}\left(\frac{\partial V}{\partial \Phi}\right)^{2/3}\left[V_L \frac{\partial K}{\partial \Phi} + \frac{\partial Q_e}{\partial \Phi} + \frac{\partial V}{\partial \Phi} \times \left(-\Gamma \frac{\partial p_i}{\partial \Phi} + Q_{\Delta e} + S_e - R_e\right)\right] \tag{4}$$

where the time derivatives are with respect to surfaces containing fixed toroidal flux [7, 8].

In Eqs (2)–(4), the quantities being advanced in time are the differential electron number density, $N' = n_e \partial V/\partial \Phi$, and the differential total and electron entropy densities,

$\sigma = p(\partial V/\partial\Phi)^{5/3}$ and $\sigma_e = p_e(\partial V/\partial\Phi)^{5/3}$. The derivative $\partial V/\partial\Phi$ is the differential volume element

$$\frac{\partial V}{\partial \Phi} = \frac{\partial}{\partial \Phi} \oint d\tau = \frac{1}{q} \oint \frac{d\ell}{B_p} \tag{5}$$

and p and p_e are the total and electron pressures. Also,

$$V_L = \frac{2\pi \langle \vec{E} \cdot \vec{B} \rangle}{\langle B \cdot \nabla \phi \rangle} \tag{6}$$

is the loop voltage and

$$K = \oint \vec{B}_p \cdot \vec{d\ell} = \oint \frac{d\ell\, |\nabla \Psi|}{R} \tag{7}$$

is the total toroidal current within a flux surface.

The ion and electron heat fluxes are defined as

$$Q_i = \frac{\partial V}{\partial \Phi} \left(\langle \vec{q}_i \cdot \nabla \Phi \rangle + \tfrac{5}{2} p_i \Gamma \right) \tag{8}$$

$$Q_e = \frac{\partial V}{\partial \Phi} \left(\langle \vec{q}_e \cdot \nabla \Phi \rangle + \tfrac{5}{2} p_e \Gamma \right) \tag{9}$$

where $\vec{q}_e$ and $\vec{q}_i$ are the random heat flux vectors, Γ denotes particle flux, and the standard definition of the flux surface average operator is used:

$$\langle a \rangle = \frac{\oint (d\ell/B_p) a}{\oint (d\ell/B_p)}$$

The plasma is assumed to have two temperatures: T_e for the temperature of the electrons of density n_e, and T_i for the temperature of the bulk ions of charge Z_i, mass M_i and density n_i. A single impurity ion of charge Z_I, mass M_I and density n_I is assumed.

Pressures, densities and temperatures are related in the standard way:

$$k_B T_e = p_e/n_e \tag{10}$$

$$k_B T_i = p_i/(n_i + n_I) \tag{11}$$

with $k_B = 1.60 \times 10^{-19}$ J/eV. Also, from charge neutrality, we have

$$n_e = Z_i n_i + Z_I n_I \tag{12}$$

The effective charge $\bar{Z}$ and the equipartition charge $\langle Z \rangle$ are defined as

$$\bar{Z} = (n_i Z_i^2 + n_I Z_I^2)/n_e \tag{13}$$

$$\langle Z \rangle = (n_i Z_i^2/M_i + n_I Z_I^2/M_I)/(n_e/M_H) \tag{14}$$

where M_H is the proton mass.

2.1. Resistivity and equipartition

The equipartition term appearing in Eq. (4) is given [9] by

$$Q_{\Delta e} = \frac{3}{2} \left[p_i - \frac{(n_i + n_I)}{n_e} p_e \right] \Big/ \tau_{\Delta e} \tag{15}$$

where

$$\tau_{\Delta e}^{-1}\,[s^{-1}] = 3.1 \times 10^{-11}\, n_e\,[m^{-3}]\, \eta_c\,[\Omega \cdot m]\, \langle Z \rangle$$

and η_c is the classical plasma resistivity for a hydrogen plasma, given by (see Ref. [9])

$$\eta_c\,[\Omega \cdot m] = (1.03 \times 10^{-4}) \ln \Lambda\, (T_e[eV])^{-3/2} \tag{16}$$

with

$$\ln \Lambda = 17.1 - \ln \{ (n_e[m^{-3}])^{1/2}\, (T_e[eV])^{-1} \}$$

Neoclassical corrections to the resistivity are assumed. These are given [10] by

$$(\eta_c/\eta_{NC}) = \Lambda_E(\bar{Z}) \left(1 - \frac{f_t}{1 + \xi(\bar{Z}) \nu_{*e}} \right) \times \left(1 - \frac{C_R(\bar{Z}) f_t}{1 + \xi(\bar{Z}) \nu_{*e}} \right) \tag{17}$$

where

$$\Lambda_E(\bar{Z}) = \frac{3.40}{\bar{Z}} \left(\frac{1.13 + \bar{Z}}{2.67 + \bar{Z}} \right)$$

$$C_R(\bar{Z}) = \frac{0.56}{\bar{Z}} \left(\frac{3.0 - \bar{Z}}{3.0 + \bar{Z}} \right)$$

$$\xi(\bar{Z}) = 0.58 + 0.20\bar{Z}$$

and the electron collisionality parameter is evaluated as

$$\nu_{*e} = (10.2 \times 10^{16})^{-1}\, R_0[m]\, q n_e[m^{-3}]\, \Lambda / f_t \delta (T_e[eV])^2$$

Here, the local inverse aspect ratio is evaluated as $\delta = a/R_0$, where

$$a = [V/(2\pi^2 R_0)]^{1/2}$$

V is the volume inside a given magnetic surface and R_0 is the radius of the magnetic axis. The trapped particle fraction f_t is evaluated in terms of surface averages over the magnetic surfaces [7] as follows:

$$f_t = 1 + \langle B^2 \rangle \langle B^{-2} \rangle + \tfrac{3}{2} \langle B^2 \rangle \langle B^{-2} [(1 - B/B_c)^{1/2} - \tfrac{1}{3}(1 - B/B_c)^{3/2}] \rangle \tag{18}$$

where B_c is the maximum value of B on a given flux surface.

In the absence of other forms of current drive, the parallel electric field is the sum of two terms — the

resistive diffusion term and the bootstrap current drive term. Thus,

$$\vec{E}\cdot\vec{B} = \eta_{\parallel}[\vec{J}\cdot\vec{B} - \vec{J}_{BS}\cdot\vec{B}] \tag{19}$$

Here,

$$\vec{J} = \mu_0^{-1}\nabla \times \vec{B} \tag{20}$$

is the total current density, and $\vec{J}_{BS}$ is the bootstrap current density given [11] by

$$\vec{J}_{BS}\cdot\vec{B} = -gp_e\left\{N_1\left[\frac{p_e'}{p_e} + \frac{1}{\bar{Z}}\frac{p_i}{p_e} \times \left(\frac{p_i'}{p_i} + \alpha_i\frac{T_i'}{T_i}\right)\right] - N_2 T_e'/T_e\right\}\Big/ D \tag{21}$$

with the definitions

$$N_1 = f_x(0.754 + 2.21\bar{Z} + \bar{Z}^2) + f_x^2(0.348 + 1.24\bar{Z} + \bar{Z}^2)$$

$$N_2 = f_x(0.884 + 2.07\bar{Z})$$

$$D = 1.414\bar{Z} + \bar{Z}^2 + f_x(0.754 + 2.657\bar{Z} + 2\bar{Z}^2) + f_x^2(0.348 + 1.234\bar{Z} + \bar{Z}^2)$$

$$\alpha_i = -1.172/(1.0 + 0.462 f_x)$$

$$f_x = f_t/(1 - f_t)$$

A simple modification of the neoclassical resistivity theory has been used in the calculations presented here to take into account the effect of the sawtooth instability on the evolution of the plasma. There are sawtooth models which attempt to resolve in time the occurrence of each sawtooth event [12, 13]. Rather than incorporate one of these models, which would necessitate resolving the evolution of the equilibrium on the rapid time-scale of the sawtooth period and crash, we utilize a time average model that consists of enhancing the resistivity inside the magnetic surface for which q = 1. We introduce the parameter a_{120} ($0 < a_{120} \leq 1$), which represents the degree by which the resistivity profile, and hence the steady state current profile, is flattened inside the sawtooth inversion radius. In terms of this parameter, the sawtooth model can be described as

$$\eta_{\parallel} = \eta_{NC} \quad \text{for} \quad q \geq 1 \tag{22}$$

$$\eta_{\parallel} = a_{120}\eta_{NC} + (1 - a_{120})\eta_{NC}|_{q=1} \quad \text{for} \quad q < 1$$

A discussion of the TSC 'averaged' model and a comparison with the Kadomtsev reconnection model [12] is given in the Appendix, where it is argued that the volt-second consumption predicted by these two models should be the same.

2.2. Thermal conductivity

The random heat flux contributions to Q_i and Q_e in Eqs (8) and (9) are evaluated using a general geometry formulation of the Coppi–Tang transport model. In this model, the electron heat flux and the ion heat flux depend only on their own respective temperature gradients. Thus, the random heat fluxes are of the form

$$\langle\vec{q}_i\cdot\nabla\Phi\rangle = -\chi_i\,|\nabla\Phi|^2\,n_i\frac{\partial T_i}{\partial\Phi} \tag{23a}$$

$$\langle\vec{q}_e\cdot\nabla\Phi\rangle = -\chi_e\,|\nabla\Phi|^2\,n_e\frac{\partial T_e}{\partial\Phi} \tag{23b}$$

The electron and ion thermal conductivities are taken to be of the following form (see Ref. [6]):

$$|\nabla\Phi|^2\,\chi_e = f_m(\chi_{TEM}^2 + \chi_{\eta i}^2)^{1/2}\,F(\Phi) \tag{24}$$

$$\chi_i = a_{126}\chi_e \tag{25}$$

where a_{126} is a constant parameter and $F(\Phi)$ is a profile factor given by

$$F(\Phi) = 8\pi^2\frac{P(\Phi)}{P(\Phi_b)}\frac{n_e(0)}{n_e(\Phi)}\frac{R_0\Phi_b}{(\partial V/\partial\Phi)} \times \exp[\tfrac{2}{3}\alpha_q\Phi/\Phi_b] \tag{26}$$

Here, Φ_b is the toroidal flux at the plasma boundary, $P(\Phi)$ is the total heating power (including Ohmic heating) minus the total radiated power inside the surface Φ, and α_q is taken to be

$$\alpha_q = q_{95} + 0.5 \tag{27}$$

where q_{95} is the safety factor at the surface containing 95% of the toroidal flux between the magnetic axis and the plasma edge. We limit α_q to lie between 2.5 and 6.5 in order to avoid unphysical results in regimes where the assumptions underlying the transport model presented here are not valid.

The functional form of the profile factor $F(\Phi)$ given in Eq. (26) follows from the insertion of the empirical steady state temperature profile

$$T(\Phi)/T(0) = \exp[-\tfrac{2}{3}\alpha_q\Phi/\Phi_b]$$

into the steady form of Eq. (3), and using the definitions in Eqs (8), (9) and (23) to solve χ_e and χ_i. It is a generalization to arbitrary geometry of the form first suggested by Coppi [2].

From Ref. [3] we obtain multipliers for the two confinement regimes:

$$\chi_{TEM} = a_{122}(1.25 \times 10^{20}) \frac{a}{n(\Phi_b)} (RB_T)^{0.3} \bar{Z}^{0.2} \times (1 + \tfrac{1}{4}\alpha_n) R^{-2.2} q_{95}^{-1.6} \quad (28)$$

$$\chi_{\eta_i} = a_{121} (7.5 \times 10^8) \left[\frac{P(\Phi_b)}{n(\Phi_b)}\right]^{0.6} (RB_T q_{95})^{-0.8} a^{-0.2} \quad (29)$$

These are combined in accordance with Eq. (24).

The factor f_m in Eq. (24) is used to account for the time averaged effect of the sawtooth instability in causing additional flattening of the temperature profile inside the $q = 1$ surface. Thus, in addition to the prescription given in Eq. (22) for modifying the resistivity profile, the sawtooth model is completed by enhancing the thermal conductivity inside the sawtooth inversion radius according to the prescription

$$f_m = 1 \quad \text{for } q > 1$$
$$f_m = a_{124} \quad \text{for } q < 1 \quad (30)$$

2.3. Particle transport

In all of the simulations presented below, the particle flux Γ appearing in Eqs (2), (4), (8) and (9) was set to zero:

$$\Gamma = 0 \quad (31)$$

The source term S_N in Eq. (2) was continuously adjusted so that the electron density profile $n_e(\Phi)$ matches both the experimentally measured line averaged density and the central density, where the experimental data were digitized every 0.0002 s. This matching was achieved by assuming a density profile of the form

$$n_e(\Phi, t) = n_e^0(t) [1 - \tilde{\Psi}^{\beta_N}]^{\alpha_N(t)} + n_b(t) \quad (32)$$

where $\tilde{\Psi}$ is the normalized poloidal flux which varies between 0 at the magnetic axis and 1 at the plasma boundary, and $n_b(t)$ is the density at the plasma boundary. In these studies, we set $\beta_N = 1.0$ and $n_b = 0.3 n_e^0$, and adjusted $n_e^0(t)$ and $\alpha_N(t)$ to match the experimental data.

This approach to modelling the density evolution was adopted for several reasons. One reason is that we are unaware of a satisfactory dynamic particle transport model for the density profile. Even if such a model did exist, it would be very difficult to infer the actual source S_N in the presence of both gas fuelling and recycling under actual conditions. Note that for the derivation used in obtaining the thermal conductivity form factor, Eq. (26), we assumed that $\Gamma = 0$, so that these two assumptions are consistent.

2.4. Radiation and impurities

In the simulations reported, it was assumed that the dominant radiation was from fully stripped ions. The surface averaged radiated power density is computed [14] as

$$R_e(\Phi, t) = 1.7 \times 10^{-38} (n_e(\Phi, t)[m^{-3}])^2 \times \bar{Z}(t) (T_e(\Phi, t)[eV])^{1/2} \quad (33)$$

The variation of the effective charge with time, $\bar{Z}(t)$, was computed from visible bremsstrahlung, assuming the radial dependence to be flat. When the dominant impurity is taken to be carbon, $Z_I = 6$, the ratio of impurity density to ion density, n_I/n_i, is defined from Eq. (14).

2.5. Boundary conditions

The boundary conditions required for TSC are of two kinds: (i) electromagnetic boundary conditions needed to evolve the magnetic field and hence define the magnetic geometry, and (ii) transport boundary conditions for the surface average densities and temperatures.

The magnetic boundary conditions are largely defined by using the experimentally measured currents

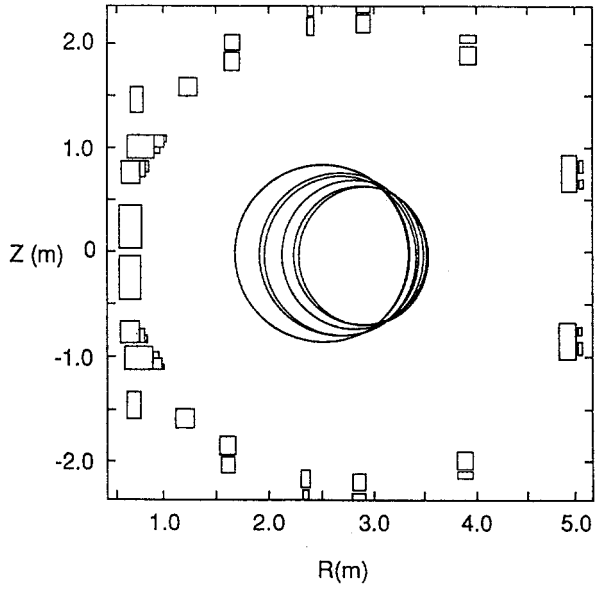

FIG. 1. Locations of the PF coils in TFTR, listed in Table I (indicated by boxes). Also shown are the plasma–vacuum interfaces at various times during the discharge simulation.

TABLE I. CO-ORDINATES OF THE POLOIDAL FIELD COILS IN TFTR

R (m)	Z (m)	Turns	ΔR (m)	ΔZ (m)
OH coils				
0.6668	0.2451	100	0.1924	0.4070
0.6703	0.7688	40	0.1721	0.1992
0.7797	0.8020	7	0.0486	0.1328
0.8162	0.8351	2	0.0243	0.0664
0.7551	1.0133	71	0.2576	0.2162
0.9108	0.9863	4	0.0566	0.0541
0.9250	1.0673	11	0.0850	0.1081
0.9816	1.0943	2	0.0283	0.0541
1.1980	1.5861	26	0.1706	0.1717
1.6040	1.8424	18	0.1433	0.1580
2.3324	2.1380	9	0.0592	0.1547
2.8390	2.3040	5	0.1217	0.0462
3.8798	2.0860	6	0.1549	0.0655
4.9997	0.7101	2	0.0372	0.0696
EF coils				
2.8403	2.1694	-9	0.1028	0.1550
3.8785	1.9471	-14	0.1547	0.1560
4.8809	0.8088	-26	0.1467	0.3428
VC coils				
0.7170	1.4650	27	0.1220	0.2339
1.6046	2.0202	-15	0.1269	0.1443
2.3326	2.2959	-4	0.0503	0.0888
4.9997	0.8748	3	0.0372	0.1090

in the four coil systems in TFTR: the Ohmic heating system $I_{OH}(t)$, the equilibrium field system $I_{EF}(t)$, the variable curvature field system $I_{VC}(t)$ and the toroidal field system $I_{TF}(t)$. Figure 1 shows a layout of the poloidal field coils in TFTR. The co-ordinates of each of the poloidal field coils are listed in Table I.

The experimental currents were modified in two ways for the simulations reported here:

(1) A plasma current control feedback system was used in the simulation in which a fictitious loop voltage, $V_f(t)$, was added to the computational boundary at each time step in order to force the plasma current in the simulation to match the experimental plasma current. The time integral of this, $\int V_f(t)dt = \Delta\Psi_s^{PF}$, represents the error of the simulation in reproducing the experimental volt-second consumption.

(2) A similar feedback system was used in the simulation to add a small correction to the equilibrium field system current, $I_{EF}(t)$, in order to force the plasma major radius in the simulation to match the experimental value $R_p(t)$. Again, this feedback correction, $\delta I_{EF}(t)$, is a measure of the error in the simulation.

The TFTR limiters can be represented by two circular arc segments: an inner one, with major radius R = 2.661 m and minor radius a = 1.01 m, and extending for 1.047 rad; and an outer one, with R = 2.601 m and a = 0.990 m, and extending for 2.043 rad. We define the plasma boundary as being the innermost magnetic flux surface that makes

TABLE II. SUMMARY OF SIMULATION AND EXPERIMENTAL RESULTS FOR DISCHARGES AT $0.05 \leq t \leq 4.5$ s

			Volt-seconds			Maximum temperature (keV)			
Discharge No.	I_p^{MAX} (MA)	n_e^0 (10^{14} m^{-3})	Total	Resistive	$\Delta\Psi_s^{PF}$	$T_{e(0)}^{EXP}$	$T_{e(0)}^{SIM}$	$T_{i(0)}^{EXP}$	$T_{i(0)}^{SIM}$
24088	2.2	0.35	16.2	3.4	0.01	4.4	4.4	2.9	3.4
24095	2.2	0.35	16.1	3.6	-0.10	4.4	4.5	3.0	2.9
24096	2.2	0.65	16.4	3.4	-0.12	3.8	3.5	3.0	3.0
24098	1.8	0.30	14.2	3.4	0.06	4.5	4.2	3.1	3.1
24100	1.8	0.70	14.2	3.3	-0.33	4.0	3.6	3.2	2.9
24093	1.4	0.37	12.3	3.2	0.45	3.4	3.4	2.7	2.7
24089	1.0	0.66	11.3	3.4	-0.20	2.5	2.8	2.2	2.3

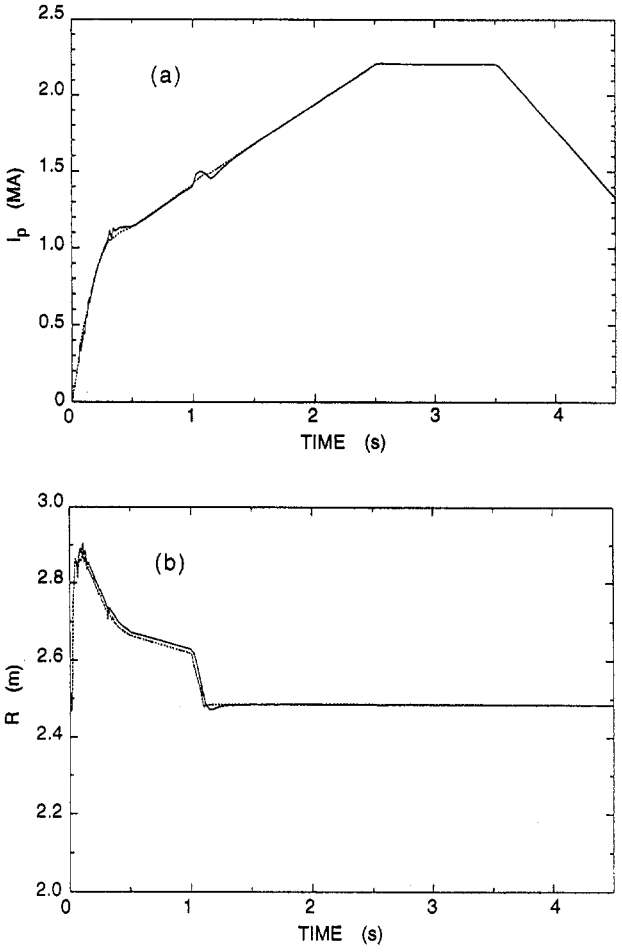

FIG. 2. (a) Plasma current and (b) major radius versus time. Comparison of the TSC simulation data (——) and the experimental data (·····). The agreement is aided by feedback on the OH and EF systems, as explained in Section 2.5.

contact with one of these limiter surfaces. At the plasma boundary we apply the boundary condition that the electron density is 30% of its central value and that both the electron and the ion temperatures are equal to the 'vacuum temperature', an input variable for TSC which we set to between 2 and 4 eV.

2.6. Free parameters

In the simulation model, there are five free parameters, which are best determined by calibrating the simulation results with experimental data. These parameters and the equation numbers where they were introduced are: a_{120} (Eq. (22)), which describes resistivity flattening inside the q = 1 surface; a_{126} (Eq. (25)), which is the ratio of the ion to electron thermal conductivity; a_{122} (Eq. (28)) and a_{121} (Eq. (29)), which are the coefficients for the TEM and the η_i induced transport; and a_{124} (Eq. (30)), which describes the additional flattening of the temperature profile inside the q = 1 surface.

In all the simulations presented here, we have used the following values for these parameters:

$$\begin{aligned} a_{120} &= 0.10 \\ a_{121} &= 0.08 \\ a_{122} &= 0.40 \\ a_{124} &= 4.00 \\ a_{126} &= 1.00 \end{aligned} \qquad (34)$$

3. EXPERIMENTAL COMPARISONS

We report here on the success of the TSC simulation model (described in Section 2) in reproducing the time dependence of seven ohmically heated helium discharges in TFTR. These discharges, which ranged in peak plasma current from 1.0 to 2.2 MA and in central density from 0.30 to 0.70 × 10^{20} m^{-3}, were all used in the parallel resistivity study reported in Ref. [15]. Their parameters are listed in Table II.

The evolution of the plasma current I_p and the major radius R for shot 24095 is shown in Fig. 2. (The evolution of the other six shots considered here is qualitatively similar). The simulation time ranges from 0.05 to 4.50 s after plasma initiation. The plasma current was ramped at approximately 3.0–5.0 MA/s until it reached a value of 1 MA, at which point the ramp rate was decreased to about 0.5 MA/s until the current reached its flat-top value. The 1.0 MA/s current rampdown began at 3.5 s. As indicated in Fig. 2 and shown also in Fig. 1, the plasma is grown off the outer limiter. During the current rampup the minor radius increases from 0.60 m to 0.83 m.

Figure 3 shows the experimentally measured values and the simulation values for the effective charge $Z_{eff}(t)$, the line averaged density $\bar{n}_e(t)$ and the ratio of peak to volume averaged density $n_e^0/\langle n_e \rangle(t)$. These quantities were input into the simulation, as discussed in Sections 2.3 and 2.4. The slight differences between the simulation and the experimental curves are an artefact of the way in which these data were input into the simulation: the values of $Z_{eff}(t)$ and the density exponent $\alpha_N(t)$ were taken as piecewise linear over 0.5 s intervals, whereas the line averaged interval was 2 ms.

The results of this simulation, together with the corresponding experimental data, are shown in Figs 4–10. Figures 4 and 5 show the time history of the central electron and ion electron temperatures and their peak to average ratios. Both the central electron temperature

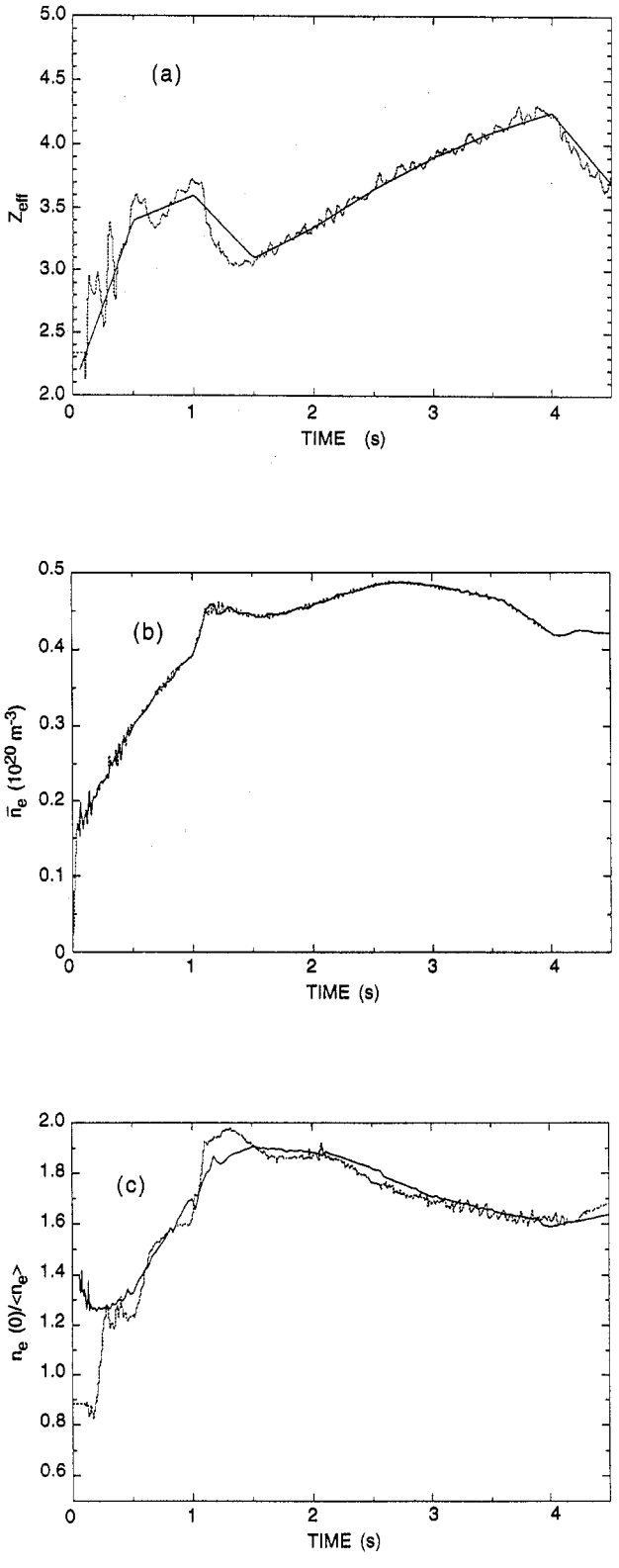

FIG. 3. Experimentally measured values (·····) and simulation values (——) of (a) the effective charge $Z_{eff}(t)$, (b) the line averaged density $\bar{n}_e(t)$, and (c) the ratio of peak to average density $n_e(0)/\langle n_e \rangle(t)$. These values were input into the simulation, as discussed in Sections 2.3 and 2.4.

and the central ion temperature in the simulation are seen to track the experimental values to within 10% for the entire duration of the simulation.

Figures 4(b) and 5(b) show that the TSC transport model is capable of tracking not only the central temperatures but also (to a large degree) the temperature profile shapes during the current rampup. Although the model slightly overestimates the peakedness of the profiles during the initial second of current rise, it correctly reproduces the time at which the profiles peak ($t \approx 1.2$ s) and the time at which they become broadest ($t \approx 3.5$ s); also it reproduces quite accurately the profile shape during the interval in between. A comparison of the temperature and density profiles across the midplane at the end of the current flat-top, $t = 3.5$ s, is given in Fig. 6.

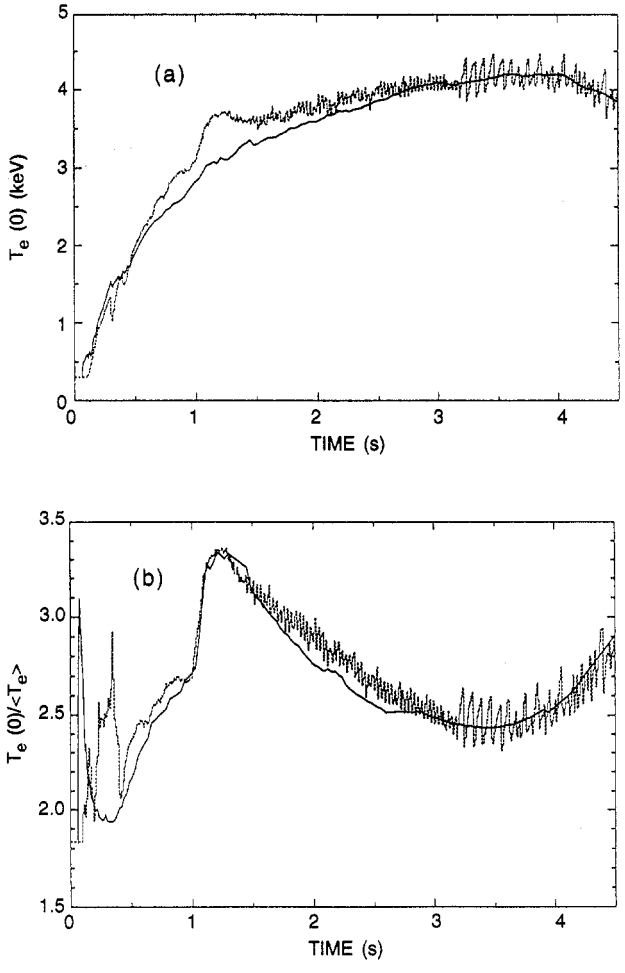

FIG. 4. Time history of the simulation values (——) and the experimental values (·····) of (a) the central electron temperature and (b) the ratio of peak to average values of electron temperature.

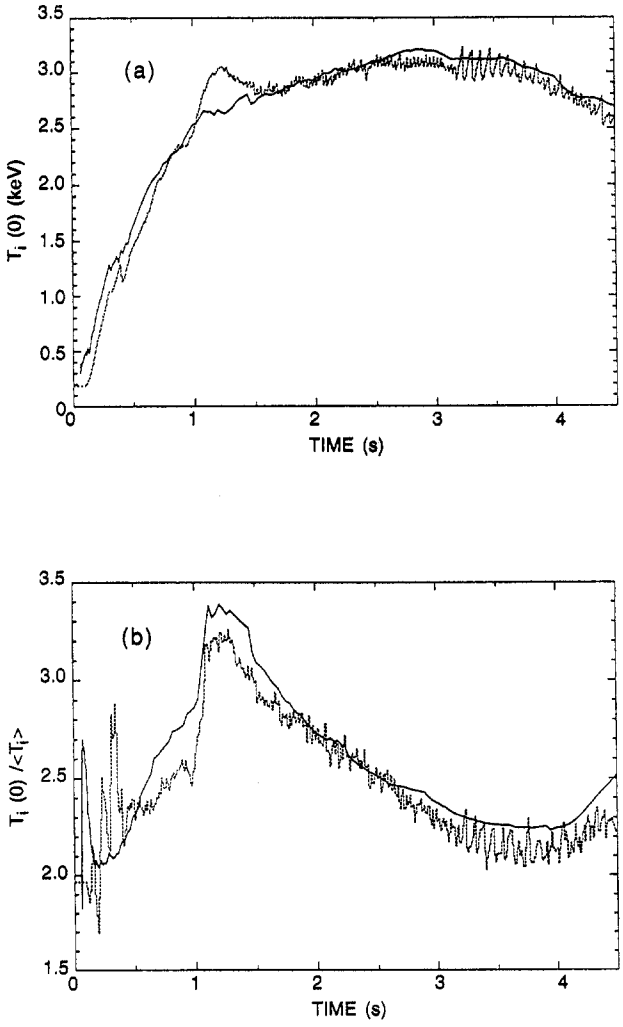

FIG. 5. Time history of the simulation values (——) and the experimental values (·····) of (a) the central ion temperature and (b) the ratio of peak to average values of ion temperature.

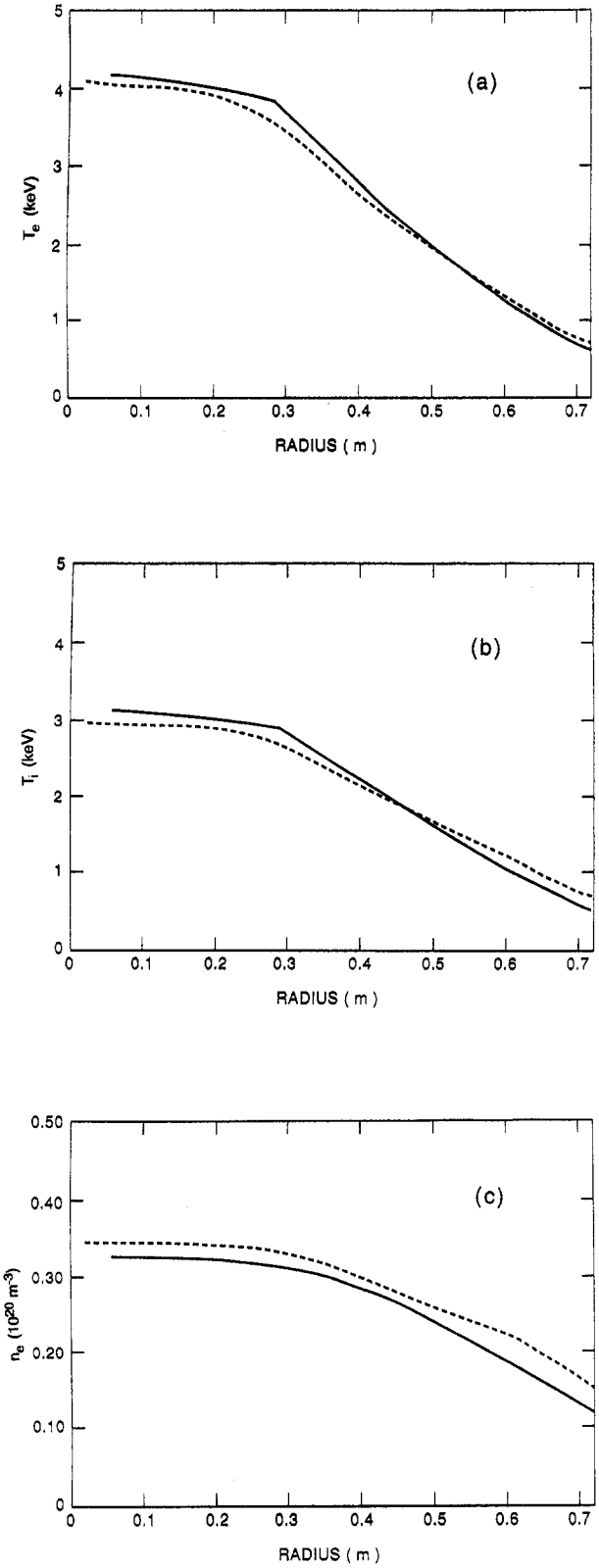

FIG. 6. Comparison of the simulation values (——) and the experimental values (·····) of (a) the electron temperature, (b) the ion temperature, and (c) the electron density versus the minor radius at t = 3.5 s.

Figure 7 presents a comparison of the total volt-seconds delivered to the plasma in the experiment (E) and the simulation (S), as well as a breakdown of the resistive (R) and the internal (I) components in the simulation. Here, the experimental curve is computed directly from the coil currents as the total flux linkage from all coils to the nominal plasma centre at $R_p = 2.65$ and $Z_p = 0$. Thus, the experimental volt-seconds is computed as

$$E = \sum_{i=1}^{N} M_{pi} \Delta I_i$$

where M_{pi} is the mutual inductance between coil i and the plasma, and ΔI_i is the amount by which the current in coil i has changed since the beginning of the simula-

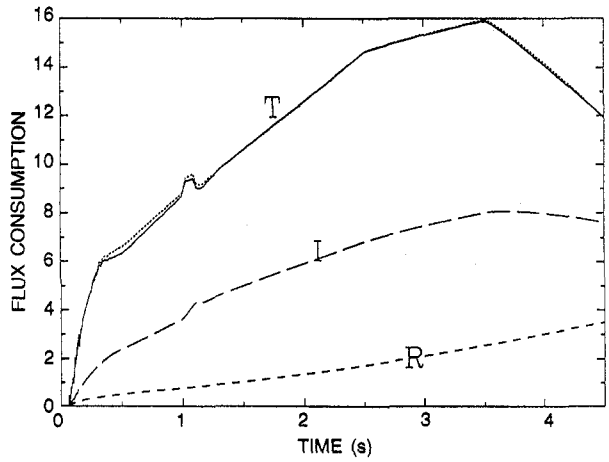

FIG. 7. Comparison of the total volt-seconds (T) delivered to the plasma in the experiment (·····) and the simulation (——). Also shown is the breakdown in the simulation between internal (I) and resistive (R) components using 'axial' accounting.

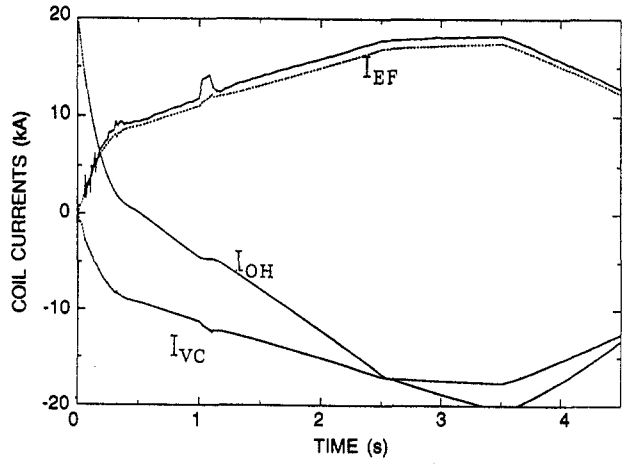

FIG. 8. Coil currents versus time for the three coil systems from the simulation (——) and the experiment (·····). I_{EF} is the equilibrium field system, I_{OH} is the Ohmic heating system and I_{VC} is the variable curvature system. The latter two were the same for the simulation and the experiment.

tion (t = 0.05 s). The total volt-seconds used in the simulation is computed as

$$S = \sum_{i=1}^{N} M_{pi}\Delta I_i + \Delta\Psi_s^{PF}$$

where $\Delta\Psi_s$ is the time integral of the additional fictitious loop voltage used in the simulation.

Also plotted in Fig. 7 is the resistive volt-second consumption in the simulation, defined as the time integral of the loop voltage on the plasma magnetic axis [16] or as the change of poloidal flux there. Thus,

$$R = \Delta\Psi_{axis}^{PF} = \int_0^t \eta_{\parallel}(0)J(0)\,dt$$

where the second equality follows from application of Faraday's law and Ohm's law (Eq. (19)). The internal volt-second curve is the change in poloidal flux at the plasma limiter,

$$I = \Delta\Psi_{limiter}^{PF}$$

Thus, the difference between the curves marked I and R is the total poloidal flux difference between the limiter and the magnetic axis at a given time.

Figures 8 and 9 show a comparison between the simulation values and the experimental values of $\Lambda = \ell_i/2 + \beta_p$ and of the currents in the equilibrium field coils, I_{EF}. The experimental curve for Λ was determined purely from magnetics measurements using the Shafranov formula. The simulation curve was calculated from computing integrals over the plasma volume using the definitions

$$\ell_i = \frac{2}{R_p\mu_0^2 I_p^2}\int B_p^2\,dV$$

$$\beta_p = \frac{4}{R_p\mu_0 I_p^2}\int p\,dV$$

Note that the simulation current in the equilibrium field coil system is the sum of the experimental value and the feedback correction, as discussed in Section 2.5,

$$I_{EF}^{Sim}(t) = I_{EF}^{Exp}(t) + \delta I_{EF}(t)$$

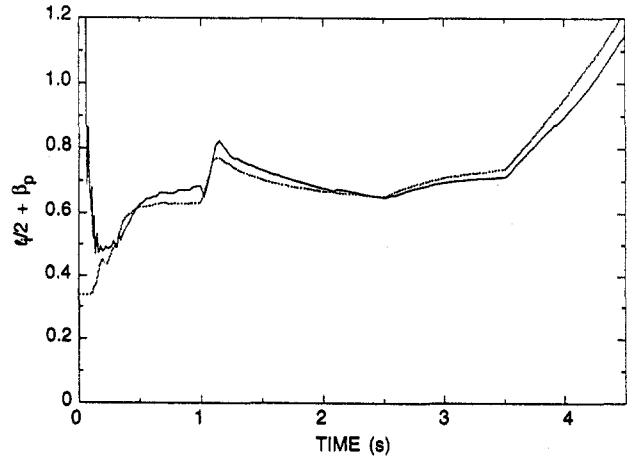

FIG. 9. Comparison between the simulation values (——) and the experimental values (·····) of $\Lambda = \ell_i/2 + \beta_p$. The experimental curve for Λ is from magnetics measurements.

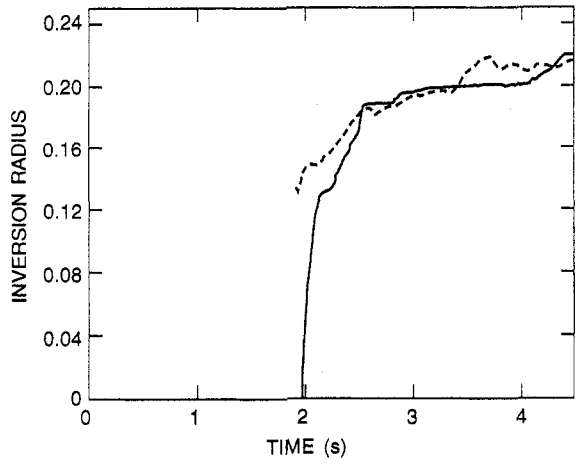

FIG. 10. Comparison between the radius of the q = 1 surface in the simulation (——) and that deduced in the experiment (·····).

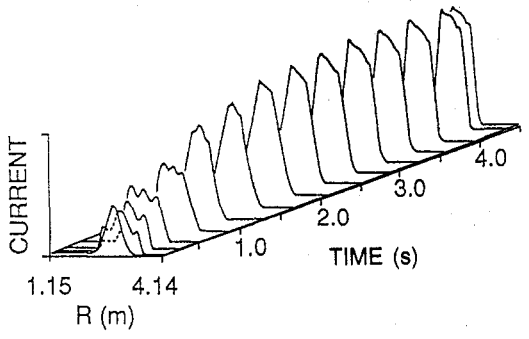

FIG. 11. Profiles of the toroidal current density plotted across the midplane z = 0 at various times during the discharge simulation.

Finally, Fig. 10 presents a comparison between the radius of the q = 1 surface computed in the simulation and that deduced experimentally by the soft X-ray camera. Figure 11 shows the computed midplane profiles of the toroidal current density. The effect of flattening of the current profile within the q = 1 surface after t = 2.0 s can be seen.

Table II summarizes the simulation and experimental results for the seven discharges studied. For each discharge the table lists the total volt-seconds required for the 4.5 s of simulation time, the axial resistive volt-second consumption in the simulation, and the difference between the experimental and the simulation volt-second consumption, $\Delta\Psi_s^{PF}$. Also listed are the maximum electron and ion temperatures obtained in the simulation and the experiment. The simulation temperatures are seen to be generally within 10% of the experimental values for the range of discharges.

The amount of resistive volt-seconds consumed in these discharges was remarkably similar, all falling within the narrow range from 3.2 to 3.6. The total volt-seconds required ranged from 11.3 for the 1.0 MA discharge to 16.4 for the 2.2 MA discharge. The absolute error in the volt-second consumption ranged from −0.3 to 0.5. This amounts to a maximum error of 4% in the total volt-seconds consumed, or an error of 15% in the resistive component.

4. DISCUSSION AND SUMMARY

The primary intent of this paper is to demonstrate that the plasma model which has been incorporated into the TSC code can reproduce many of the features of an Ohmic tokamak discharge to an accuracy close to the experimental uncertainty. These features include peak and average temperatures, current profile evolution, location of the sawtooth inversion radius and volt-second consumption. This gives us some confidence in using TSC as a design tool for predicting the volt-second consumption during the Ohmic startup phase in future experiments.

In performing the calibration runs presented here, several interesting trends were noted which are outside the original scope of this paper but which deserve mention. Probably the most important of these is that no anomalous parallel resistivity was needed to reproduce the current rampup phase. This was reported previously [15] and is confirmed by the present study.

A second observation of interest concerns the evolution of the peak to average temperature profile as illustrated in Fig. 4(b). It is seen that this ratio reaches a maximum during the current ramp at 1.1 s, which is the time when the plasma minor radius has grown to its full value (see Fig. 2). The ratio then decreases steadily until about 3.5 s, when the current ramp-down begins. This long time-scale is apparently set by the current diffusion time; it was also noted in previous publications [17].

It may well be possible to exploit the effect of this temperature profile evolution in a transient ignition experiment such as the proposed BPX [18] and IGNITOR [19] devices. The more peaked the temperature profiles, the easier it is to satisfy the ignition criteria for a D–T tokamak. By timing the current ramp and shape evolution of the discharge properly, it may well be possible to ignite the tokamak before the temperature profile broadening begins.

Appendix

Here we discuss the argument that the TSC sawtooth model described at the end of Section 2.1 (in particular by Eqs (22) and the preceding paragraph) will predict the same plasma edge loop voltage and transformer requirement for some value of the free parameter a_{120} as does the more familiar Kadomtsev [12] reconnection model. This single free parameter of the TSC sawtooth model is analogous to the single free parameter in the Kadomtsev model — the sawtooth period τ_p.

The Kadomtsev reconnection model describes a periodic phenomenon in which the plasma current inside the toroidal flux surface Φ_0 is allowed to peak so that the safety factor on axis, q_0, falls below unity. Then, at some predetermined value of q_0 (or, alternatively, after some predetermined time), the magnetic surfaces inside Φ_0 reconnect in order to flatten the current inside that surface. Typical profiles of the plasma current in the Kadomtsev model just before and just after the flattening are shown as curves 1 and 2 in Fig. A-1.

In the TSC sawtooth model, the resistivity profile is artificially flattened inside Φ_0 according to the description given in Eq. (22). This causes the plasma current inside Φ_0 to assume a steady state profile the peakedness of which is intermediate between that of the Kadomtsev model profile before the crash and that after the crash. The TSC current profile is shown in curve 3 of Fig. A-1.

We argue here that the use of the TSC sawtooth model will produce the same loop voltage at the plasma edge as does the Kadomtsev reconnection model. The TSC model has one free parameter to affect the central current peakedness (a_{120}), just as the Kadomtsev model has a free parameter to control the time averaged peakedness.

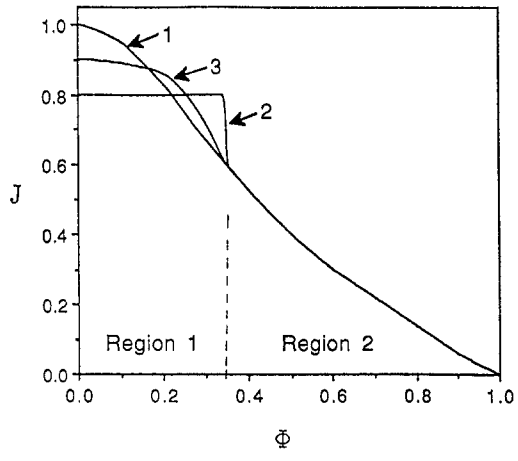

FIG. A-1. Curves 1 and 2 are the profiles of the plasma current in the Kadomtsev model before and after reconnection. Curve 3 is the current produced by the TSC 'averaged' model.

In general, the loop voltage V_L as defined in Eq. (6) is a function of the magnetic co-ordinate Φ. The time derivative of the inverse safety factor is equal to the derivative of V_L with respect to the toroidal flux

$$\frac{\partial}{\partial t} q^{-1} = \frac{d}{\partial \Phi} V_L \qquad (A.1)$$

In particular, if the q-profile is stationary in time in the outer region of the plasma (Region 2 in Fig. A-1), then the loop voltage is constant in this region with the same value of V_L as at the plasma edge. This is the voltage that must be supplied by the external transformer. Thus, from Eqs (6) and (19)–(21), the loop voltage at the plasma edge is given by

$$V_L|_{edge} = 2\pi\eta_{\parallel} \frac{\langle(\vec{J} - \vec{J}_{BS})\cdot\vec{B}\rangle}{\langle\vec{B}\cdot\nabla\Phi\rangle} \qquad (A.2)$$

where the right hand side is evaluated *anywhere* in Region 2. Therefore, we see that whatever is going on in Region 1 will not affect the loop voltage being supplied by the transformer as long as it does not affect any of the quantities in Eq. (A.2) in Region 2. This is the basis for concluding that the TSC 'averaged' model and the Kadomtsev reconnection model can give identical results for the loop voltage at the plasma boundary and hence for the volt-seconds required for a given discharge.

ACKNOWLEDGEMENTS

This work was supported by the United States Department of Energy, under Contract No. DE-AC02-76-CHO3073.

REFERENCES

[1] JARDIN, S.C., POMPHREY, N., DeLUCIA, J.L., J. Comput. Phys. **66** (1986) 481.
[2] COPPI, B., Comments Plasma Phys. Control. Fusion **5** (1980) 261.
[3] TANG, W.M., Nucl. Fusion **26** (1986) 1605.
[4] REDI, M.H., TANG, W.M., EFTHIMION, P.C., et al., Nucl. Fusion **27** (1987) 2001.
[5] ARUNASALAM, V., BRETZ, N.L., EFTHIMION, P.C., et al., On the Self-Consistency of the Principle of Profile Consistency Results for Sawtoothing Tokamak Discharges, Rep. PPPL-2609, Princeton Plasma Physics Laboratory, Princeton, NJ (1989).
[6] JARDIN, S.C., DeLUCIA, J., OKABAYASHI, M., et al., Nucl. Fusion **27** (1987) 569.

[7] HIRSHMAN, S.P., JARDIN, S.C., Phys. Fluids **22** (1979) 731.
[8] JARDIN, S.C., J. Comput. Phys. **43** (1980) 31.
[9] BOOK, D.L., NRL Plasma Formulary, NRL Publ. 0084-4040, Naval Research Laboratory, Washington, DC (1987).
[10] HIRSHMAN, S.P., HAWRYLUK, R.J., BIRGE, B., Nucl. Fusion **17** (1977) 611.
[11] HIRSHMAN, S.P., Phys. Fluids **31** (1988) 3150.
[12] KADOMTSEV, B.B., Sov. J. Plasma Phys. **1** (1975) 389.
[13] WARD, D.J., JARDIN, S.C., Nucl. Fusion **29** (1989) 905.
[14] SHEFFIELD, J., Tokamak Startup (KNOEPFEL, H., Ed.), Plenum Press, New York (1986).
[15] ZARNSTORFF, M.C., McGUIRE, K., BELL, M.G., et al., Phys. Fluids B **2** (1990) 1852.
[16] HAWRYLUK, R.J., SCHMIDT, J.A., Nucl. Fusion **16** (1976) 775.
[17] FREDRICKSON, E.D., McGUIRE, K.M., GOLDSTON, R.J., et al., Nucl. Fusion **27** (1987) 1897.
[18] JARDIN, S.C., *in Fusion Engineering* (Proc. 13th Symp. Knoxville, TN, 1989), IEEE, New York (1990) 1285.
[19] COPPI, B., and the Ignitor Program Group, in Plasma Physics and Controlled Nuclear Fusion Research 1988 (Proc. 12th Int. Conf. Nice, 1988), Vol. 3, IAEA, Vienna (1989) 357.

(Manuscript received 16 March 1992
Final manuscript received 9 November 1992)